Research Square

Preprints are preliminary reports that have not undergone peer review.
They should not be considered conclusive, used to inform clinical practice,
or referenced by the media as validated information.

Solar wind electron-streaming instability dynamics with lunar magnetic anomaly

Partha Pratim Deka
Tezpur University
Pralay Kumar Karmakar
pkk@tezu.ernet.in

Tezpur University

Research Article

Keywords: Solar-wind plasma, Streaming instability, Lunar magnetic anomaly, Linear dispersion relation

Posted Date: November 3rd, 2026

DOI: https://doi.org/10.21203/rs.3.rs-11322983/v1

License: This work is licensed under a Creative Commons Attribution 4.0 International License.
Read Full License

Additional Declarations: No competing interests reported.

Solar wind electron-streaming instability dynamics with lunar magnetic anomaly

Partha Pratim Deka, Pralay Kumar Karmakar*
Department of Physics, Tezpur University, Napaam, Tezpur 784028, Assam, India
*E-mail: pkk@tezu.ernet.in

Abstract

We analyse the electrostatic modes triggered by the electron-streaming instabilities in the magnetised solar-wind plasmas over the lunar magnetic anomalies (LMAs). A standard normal mode analysis is applied to derive a generalised linear dispersion relation to understand the observed electrostatic modes in the Moon over the LMAs. The various excited wave modes are illustratively identified and characterised. The interaction between the electron-beam mode and the normal acoustic modes, including their branch coupling and coalescence, is examined to elucidate the origin of the electron-streaming instability. We further investigate the effects of the propagation angle (θ) variation, relative to the interplanetary magnetic field (IMF), on the instability growth rate. The stabilising effects of the IMF on the instability are investigated. The consistency of this analysis in light of the existing *Kaguya* observations is finally established.

Keywords Solar-wind plasma, Streaming instability, Lunar magnetic anomaly, Linear dispersion relation

1 Introduction

The Moon is an airless body without an intrinsic global magnetic field (Dolginov et al. 1961; DOLGINOV et al. 1963). Due to its proximity to the Earth, the retention of ancient geological history (Heiken et al. 1991) without an atmosphere, and the direct interaction of solar wind with its surface, the Moon has been one of the most extensively studied bodies over the past few decades. One of the most interesting phenomena that have been spotted on the Moon's surface is the lunar swirl. These are bright, wispy patterns on the lunar surface that stand out against the otherwise dark lunar soil, like hundreds of kilometres of widespread bleach stains (Mack 2012). It has attracted considerable attention from researchers all over the world (Blewett et al. 2011; Hood and Schubert 1980; Halekas et al. 2001; Richmond and Hood 2008; Bamford et al. 2012). Many missions have confirmed that there is no global magnetic field on the Moon (DOLGINOV et al. 1963; Dolginov et al. 1961). But there are some regions on the Moon's surface that have high levels of magnetisation, referred to as lunar magnetic anomalies (LMAs) or crustal magnetic fields (CMFs) (Hood and Schubert 1980; Halekas et al. 2001; Richmond and Hood 2008; Bamford et al. 2012; Hood and Artemieva 2008; Coleman Jr 1972; Hood et al. 1979; Tsunakawa et al. 2010). These LMAs are widely believed to be remnants of an ancient global magnetic field. These regions act as mini-magnetospheres to partially shield the surface from solar winds, ultraviolet radiation, and cosmic rays [14–16]. Reiner Gamma is one prominent example of lunar swirls associated with such magnetic anomalies (Kurata et al. 2005). Most popular hypotheses offered regarding the origin of these LMAs is the giant impact hypothesis (Hartmann and Davis 1975). According to this hypothesis, the Moon’s small

metallic core is roughly 1% to 2% of its mass. The metallic core is composed of iron-deficient rocky materials from the Earth's mantle. This small size of the metallic core is a critical constraint for a lunar dynamo. Although, a global magnetic field likely existed billions of years ago, its insufficient volume caused it to cool-down and solidify rapidly. The ancient dynamo has left behind these localized magnetic anomalies frozen into the crust (Hood and Artemieva 2008; Runcorn 1994). Complementary to this, massive meteor impacts are believed to generate transient plasma clouds that amplified these fields. It imprinted magnetic signatures into the crust at the impact's antipode (Hood and Vickery 1984; Hood and Artemieva 2008; Lin et al. 1988). Recent paleointensity data and numerical simulations support the existence of an ancient dynamo with a field of approximately 1 μT about 4.2 billion years ago (Garrick-Bethell et al. 2009). If such a lunar magnetosphere existed, it may have even shielded the early Earth's atmosphere, influencing its formation and evolution (Takahashi and Tsunakawa 2009). Table 1 briefly summarises various LMAs observed in the Moon.

Table 1 Lunar magnetic anomalies: observational summary

Sl. no.	Mission/Instrument	Altitude (km)	Target anomalies	Horizontal spread (km)	Measured strength (nT)	Reference
1	Apollo 15 subsatellite	~100	Van de Graaff / Far side	~100 (spot-like anomalies)	~2–10	(Coleman Jr 1972)
2	Apollo 16 subsatellite	~100	Descartes / North ray	~50–150	~2–10	(Hood et al. 1979)
3	Lunar prospector (MAG/ER)	~20 – 30 (lowest periapsis)	Reiner Gamma / South pole-Aitken	~50–300	~50–300	(Halekas et al. 2001; Richmond and Hood 2008)
4	Surface extrapolation (Apollo + LP data)	0 (surface)	Strongest crustal sites	~50–300	~1000 (strongest anomalies)	(Hood and Artemieva 2008; Richmond and Hood 2008)
5	Kaguya (SELENE)	~10-100	Gerasimovich, Mare Ingenii, Airy	~20–150	~10–40 (at 10 km)	(Tsunakawa et al. 2010)

Solar wind originating continuously from the Sun's outer layer (corona) travels through the interstellar medium at supersonic speeds (Parker 1958). It is primarily composed of electrons, protons and a few fractions of heavier ions (Wurz 2005). The Moon takes direct hit of these energized particles. Solar wind plasma carries the Sun's magnetic field known as the interplanetary magnetic field (IMF) (Kivelson et al. 1996; Parker 1958). The IMF strength usually ranges from 5 to 10 nT at a distance of 1 AU (Hapgood et al. 1991; Kivelson et al. 1996). However, it significantly intensifies during extreme solar events like coronal mass ejection (CME) (Richardson and Cane 2010). The field orientation is determined by the Parker spiral angle (Parker 1958; Thomas and Smith 1980). It is approximately 45 degrees relative to

the Sun-Earth line at 1 AU distance (Parker 1958; Thomas and Smith 1980). The frozen field lines in the highly conductive solar wind are carried radially outward, while the Sun's rotation winds them into a spiral. This IMF together with the lunar CMF governs the magnetisation and trajectory of the solar wind plasma as it interacts with the Moon's surface.

A relative drift between constitutive charged particles in a plasma system triggers an instability known as the streaming instability, or two stream instability, or multi-stream instability (Chen 2015). The large difference in the drift energy with respect to the thermal energy in the system provides the free energy necessary for exciting various associated waves. The streaming instability plays an important role across a wide range of physical scenarios: from the aerodynamic concentration of solids into planetesimal-forming clumps in protoplanetary disks (Su et al. 2026) to the modelling of ultrarelativistic beam-plasma interactions in high-energy astrophysics (Labro et al. 2026), and even the turbulent mixing and transport processes triggered during different high-velocity celestial flybys (Lim 임 et al. 2026). In this context, Aggarwal 1979 has investigated the streaming instability in plasmas where electrons move relative to ions at an arbitrary angle to the ambient magnetic field. The magnetic field strength, orientation, and thermal effects have been reported to significantly influence the growth rates and unstable regions of the said instability.

The Moon has been viewed as a passive plasma sink that simply absorbed particles and left a void (wake) in its trail. Modern mission data from *ARTEMIS*, *Chandrayaan-1*, *Kaguya*, and *Chang'E-1* have refined this idea. These observations reveal a sophisticated and dynamic environment where the solar wind is not just absorbed, but reflected and diverted (Chu et al. 2021; Halekas et al. 2008; Saito et al. 2008a). This triggers a lot of exciting electromagnetic phenomena. Analysis of data from the *Kaguya* orbiter have revealed three distinct categories (Type A, B and C) of electrostatic solitary waves (ESWs) in the lunar plasma environments (Hashimoto et al. 2010). Out of these, Type B waves are intense signals generated by bi-streaming electrons that are mirror-reflected over the LMAs. Our study focuses on this type of electrostatic fluctuations described in Hashimoto et al. 2010. *ARTEMIS* data have been utilized to investigate the plasma environment over lunar CMFs, where the reflected solar-wind particles trigger complex wave-particle interactions (Chu et al. 2021). Electron two-stream instability (ETSI) and electron cyclotron drift instability (ECDI) are the primary drivers of the observed electrostatic waves. Reflected charged particles are found to provide the free-energy that destabilises the lunar environment.

The Moon serves as a natural laboratory for studying how airless bodies interact with the harsh solar wind and solar flares like events. Because its surface is directly exposed to plasma, the Moon mimics the electromagnetic environment that satellites and deep-space probes encounter. Counter-streaming charged particle beams reflected from CMFs have been observed to trigger various wave modes in lunar plasma environments; however, these remain underexplored from a theoretical perspective. Motivated by this gap, the present study provides a linear analysis of the electron-streaming instability triggered by the solar wind's interaction with the LMAs in the lunar sunlit side. Adopting a fluid model, appropriate for investigating the collective characteristics, we derive a 12-degree linear dispersion relation to examine various electrostatic modes. The subtle yet finite effect of the IMF strength, and orientation on the electrostatic waves triggered in the otherwise unmagnetised lunar environment are demonstrated. The impact of finite thermal velocity and the variations in streaming-electron population are also analysed. Finally, we validate our results by comparing them with observations.

2 Physical Model

When solar wind plasmas interact with the lunar CMF a fraction of the incident solar electrons reflects back towards the incident solar wind (Chu et al. 2021; Halekas et al. 2008; Hashimoto et al. 2010; Lue et al. 2011). This reflected electron-stream, together with the incoming solar wind, facilitates the ideal scenario for generation of the streaming instability (Chu et al. 2021; Hashimoto et al. 2010). As a result of this interaction, various electrostatic wave activities are observed in the lunar environment. In an attempt to theoretically explore the occurrence of these electrostatic waves, we employ a homogeneous, collisionless, and magnetised three-component fluid plasma model. It is considered to consist of fluid electrons and fluid protons only. While, heavier ions are neglected due to their comparatively lower abundance (Wurz 2005), the protons provide a neutralising background. While the incident solar electrons are assumed to be at rest with respect to the ion background, reflected electrons are considered streaming. Although, a finite Lorentz force may modify an oblique beam trajectory, the streaming instability growth time, in general, is much shorter than the electron gyro-period in weakly magnetised regime. Therefore, the beam is assumed to remain approximately unchanged during the linear growth phase. 30 % of the incident solar-wind electrons are taken to be reflected back. While this arbitrarily chosen fraction (30 %) is introduced as a parameter representing the outcome of the reflection mechanism, we also explore its systematic variation. A fully self-consistent determination of the reflected distribution is outside the scope of this present study. The thermal energy of the plasma constituents is incorporated using an approximation that neglects kinetic wave-particle interactions, such as Landau damping, thereby focusing on fluid behaviour. Fig. 1 illustrates the schematic cartoon of the system.

3 Mathematical formulations

We consider a three-dimensional (3-D) Cartesian coordinate system. The IMF ($\boldsymbol{B_0}$) is assumed to be constant and uniform along the Z-axis, which is the Sun-Moon connecting line, specifying the primary axis of the solar wind magnetisation. The basic model governing equations, comprising the continuity, momentum, and Poisson equations in a generic symbolism (Chen 2015), are respectively cast as

$$\frac{\partial n_j}{\partial t} + \boldsymbol{\nabla}.\left(n_j \boldsymbol{v_j}\right) = 0, \tag{1}$$

$$\frac{\partial \boldsymbol{v}_j}{\partial t} + (\boldsymbol{v_j}.\boldsymbol{\nabla})\boldsymbol{v}_j = \frac{q_j}{m_j}\left(\boldsymbol{E} + \frac{\boldsymbol{v_j}\times\boldsymbol{B}}{c}\right) - \frac{\boldsymbol{\nabla}\mathrm{P_j}}{m_j n_j}, \tag{2}$$

$$\boldsymbol{\nabla}.\mathbf{E} = 4\pi\Sigma q_j n_j; \tag{3}$$

where, j= i, es, and eb represent the ions, stationary electrons, and streaming beam-electrons, respectively. In the momentum equation (Eq. 2), $P_j = c_j^2 m_j n_j$, stands for the thermal pressure, where $c_{Sj} = \sqrt{k_B T_j / m_j}$ is the acoustic speed for the jth species. All other symbols have their usual meanings in the above set of equations. The role of the thermal pressure is introduced via the isothermal equation of state, where the pressure fluctuations are related to the density fluctuations via the acoustic speed c_{Sj} (Aggarwal 1979). The closure of the equation assumes that the frequency of the wave is sufficiently high to neglect the thermal conduction, as required

by the collisionless fluid approximation (Chen 2015). This thermal pressure gradient term introduces finite temperature effects while remaining within a collisionless fluid framework.

We apply the following perturbation scheme for linear analysis of the system

$$F(\boldsymbol{r},t) = F_0 + F_1(\boldsymbol{r},t), \tag{4}$$

$$F(\boldsymbol{r},t) = [n_j \quad \boldsymbol{v}_j \quad \boldsymbol{E} \quad \boldsymbol{B}]^T, \tag{5}$$

$$F_0 = [n_{j0} \quad \boldsymbol{v}_{j0} \quad 0 \quad \boldsymbol{B}_0]^T, \tag{6}$$

$$F_1(\boldsymbol{r},t) = [n_{j1} \quad \boldsymbol{v}_{j1} \quad \boldsymbol{E}_1 \quad 0]^T. \tag{7}$$

We consider the perturbations to be of the form, $F_1(\boldsymbol{r},t) \sim e^{i(\boldsymbol{k}.\boldsymbol{r}-\omega t)}$. Here, equilibrium values and the first order perturbations are denoted by the subscripts 0 and 1, respectively. Applying these perturbations to the set of governing equations (Eqs. 1-3) around the equilibrium we obtain the following linearised set of equations:

$$n_{j1} = \left(\frac{n_{j0}}{\omega_{jd}}\right)\boldsymbol{k}.\boldsymbol{v}_{j1}, \tag{8}$$

$$\omega_{jd}^2\boldsymbol{v}_{j1} - i\omega_{jd}\left(\frac{q_j}{m_j}\right)\left(\boldsymbol{E}_1 + \frac{\boldsymbol{v}_j\times\boldsymbol{B}_1}{c}\right) - i\omega_{jd}\left(\boldsymbol{v}_{j1}\times\boldsymbol{\Omega}_j\right) - c_{sj}^2\boldsymbol{k}\left(\boldsymbol{k}.\boldsymbol{v}_{j1}\right) = 0, \tag{9}$$

$$k^2\phi = 4\pi\Sigma q_j n_{j1}. \tag{10}$$

The parameters ω_{jd}, and $\boldsymbol{\Omega}_j$ appearing in Eqs. 8–10 denote the Doppler-shifted angular frequency and gyrofrequency, respectively. These quantities are defined by the following expressions:

$$\omega_{jd} = \omega - \boldsymbol{k}.\boldsymbol{v}_{j0}, \tag{11}$$

$$\boldsymbol{\Omega}_{\mathrm{j}} = \frac{q_j\boldsymbol{B_0}}{m_j c}. \tag{12}$$

Substituting v_{j1} from Eq. 9 into Eq. 8 we obtain,

$$n_{j1} = \left(\frac{n_{j0}}{\omega_{jd}}\right)\frac{\omega_{jd}(q_j/m_j)k^2\phi\left\{\omega_{jd}^2-\left(\boldsymbol{k}.\boldsymbol{\Omega}_j\right)^2/k^2\right\}}{\omega_{jd}^2\left(\omega_{jd}^2-\Omega_{\mathrm{j}}^2\right)-c_{Sj}^2k^2\left(\omega_{jd}^2-\left(\boldsymbol{k}.\boldsymbol{\Omega}_j\right)^2/k^2\right)}. \tag{14}$$

Inserting n_{j1} from Eq. 14 into the linearised Poisson equation (Eq. 10) we obtain,

$$\sum_j \omega_{pj}^2\left\{\omega_{jd}^2 - \frac{\left(\boldsymbol{k}.\boldsymbol{\Omega}_j\right)^2}{k^2}\right\}\left\{\omega_{jd}^2\left(\omega_{jd}^2-\Omega_j^2\right) - k^2c_{sj}^2\left(\omega_{jd}^2 - \frac{\left(\boldsymbol{k}.\boldsymbol{\Omega}_j\right)^2}{k^2}\right)\right\}^{-1} = 1. \tag{15}$$

This is the generalised linear dispersion relation (Eq. 15) for our system and structurally resemble to the one derived in Aggarwal 1979. Now, for waves propagating along the streaming direction ($k \parallel \boldsymbol{v_{j0}}$) but inclined to the magnetic field ($\boldsymbol{B_0}$), Eq. 15 for all species becomes,

$$\frac{\omega_{pi}^2\{\omega^2-\Omega_i^2\cos^2\theta\}}{\omega^2\left(\omega^2-\Omega_{\mathrm{i}}^2\right)-c_{Si}^2k^2(\omega^2-\Omega_i^2\cos^2\theta)} + \frac{\omega_{pes}^2\{\omega^2-\Omega_e^2\cos^2\theta\}}{\omega^2\left(\omega^2-\Omega_{\mathrm{e}}^2\right)-c_{Se}^2k^2(\omega^2-\Omega_e^2\cos^2\theta)} + \frac{\omega_{peb}^2\{(\omega-ku)^2-\Omega_e^2\cos^2\theta\}}{(\omega-ku)^2\left((\omega-ku)^2-\Omega_{\mathrm{e}}^2\right)-c_{Se}^2k^2((\omega-ku)^2-\Omega_e^2\cos^2\theta)} = 1\,. \tag{16}$$

Here, θ is the angle made by both the wave vector ($\boldsymbol{k}$) and the electron-streaming direction ($\boldsymbol{v_{eb0}} = \boldsymbol{v_0}$) with the magnetic field ($\boldsymbol{B_0}$). This assumption restricts the present analysis to

electrostatic two-stream modes. Oblique beam-wave configurations ($\boldsymbol{k} \nparallel \boldsymbol{v}_0$), which may introduce additional branches, are beyond the focus of the present study. Eq. 16 is the unnormalised 12-degree linear dispersion relation. We apply the standard normalisation procedure to make the system dimensionless. The normalisation scheme is summarised in Table 2. The frequency normalising parameter, ω_{pe} represents the collective electron-plasma frequency derived from the sum of both stationary, and streaming-electron populations ($\omega_{pe}^2 = \omega_{pes}^2 + \omega_{peb}^2$). The normalised dispersion relation becomes,

$$\frac{\delta^2\left\{\omega^{*2}-\Omega_i^{*2}\cos^2\theta\right\}}{\omega^{*2}\left(\omega^{*2}-\Omega_i^{*2}\right)-c_{Si}^{*2}k^{*2}(\omega^{*2}-\Omega_i^{*2}\cos^2\theta)}+\frac{f_{es}\left\{\omega^{*2}-\Omega_e^{*2}\cos^2\theta\right\}}{\omega^{*2}\left(\omega^{*2}-\Omega_e^{*2}\right)-c_{Se}^{*2}k^{*2}(\omega^{*2}-\Omega_e^{*2}\cos^2\theta)}+\frac{f_{eb}\left\{(\omega^*-k^*)^2-\Omega_e^{*2}\cos^2\theta\right\}}{(\omega^*-k^*)^2\left((\omega^*-k^*)^2-\Omega_e^{*2}\right)-c_{Se}^{*2}k^{*2}\left((\omega^*-k^*)^2-\Omega_e^{*2}\cos^2\theta\right)}=1. \quad (17)$$

Here, $\delta^2 = m_e/m_i$ represents the square of the electron-to-ion mass ratio, while $f_{es} = n_{es}/n_{e0}$ and $f_{eb} = n_{eb}/n_{e0}$ denote the density fractions of stationary electrons and streaming-electrons, respectively. Also, it is to be noted that $f_{es} + f_{eb} = 1$. we numerically solve Eq. 17 to analyse for various modes triggered in the system.

Table 2 Normalisation scheme and normalised values

Sl. No.	Physical parameter	Normalising parameter	Normalised parameter	Typical value of the normalising parameter
1	Frequency ($\omega, \omega_{pes}, \omega_{peb}, \omega_{pi}, \Omega_e, \Omega_i$)	Electron plasma frequency (ω_{pe})	$\omega^*, \omega_{pes}^*, \omega_{peb}^*$ $\omega_{pi}^*, \Omega_e^*, \Omega_i^*$	1.26×10^5 rad s^{-1}
2	Velocity (c_{Se}, c_{Si})	Streaming velocity (v_o)	c_{Se}^*, c_{Si}^*	1.32×10^6 ms^{-1}
3	Oscillation wavenumber (k)	Wavenumber (ω_{pe}/v_o)	k^*	0.95×10^{-1} m^{-1}

4 Results and discussions

We numerically solve the normalised linear dispersion relation (Eq. 17) obtained in the previous section. The IMF exhibits a broad dynamic range, which has a baseline ranging from $5 - 10$ nT for quiet solar wind conditions (Hapgood et al. 1991). However, during active solar events such as major interplanetary coronal mass ejections (ICMEs), including the "Mother's Day" storm (experienced in May 2024), this range can be significantly enhanced, occasionally reaching values on the order of $\sim 30 - 60$ nT (Kruparova et al. 2024). The highest end of this solar-driven magnetic disturbances is occupied by 1-in-80-year superstorms such as the 1859 Carrington Event, which have peak IMF magnitudes of $90 - 110$ nT (Cid et al. 2015; Li et al. 2006). In this study, we adopt $10 - 60$ nT magnetic field range to explore the dynamics in a slightly strong magnetisation. The analysis moves beyond the quiet-time baseline ($5 - 10$ nT) to investigate how increased Lorentz force and cyclotron frequencies influence the stability and dispersion characteristics of the plasma. This yields the normalised electron and ion gyrofrequency ranges as $0.014 - 0.084$ and $7.62 \times 10^{-6} - 4.57 \times 10^{-5}$ for $10 - 60$ nT field strength, respectively. On the other hand, we consider $T_e \approx 10T_i$, which lies within the

upper range of electron-to-ion temperature ratios observed in the solar wind and is frequently encountered in the near-lunar plasma environment, particularly within the lunar wake and over the LMAs (Halekas et al. 2011; Kasper et al. 2003; Maksimovic et al. 2005; Saito et al. 2008b). Along with this, we consider the electron-streaming velocity to be $v_0 = 1.32 \times 10^7$ ms^{-1}. This value of velocity is derived from a representative energy of 0.5 keV from the MAP/PACE diagrams in the study by Hashimoto et al. 2010. Using this, we obtain electron and ion thermal velocities, normalised by the streaming velocity, to be 0.10 and 0.00074, respectively.

The analyses are conducted for three separate propagation angles ($0°, 60°$ and $90°$), allowing for a systematic comparison between parallel, oblique, and perpendicular propagation regimes. The physical model requires an anti-parallel streaming configuration (i.e., $90° \leq \theta \leq 180°$) to represent particles reflected back into the solar wind. The symmetry under the transformation $\theta \rightarrow 180° - \theta$, due to the $\cos^2\theta$ dependence on the dispersion relation (Eq. 17), allows us to interpret the parallel and anti-parallel configurations numerically equivalent. Therefore, we restrict our analyses to the interval $(0°, 90°)$, with the understanding that this symmetry arises from the mathematical structure of the model rather than a strict physical equivalence. We start with the zero thermal velocity ($c_{Se}^* = c_{Si}^* = 0$) case and subsequently investigate how finite thermal velocity influences the instability.

Fig. 2 is a graphical representation of the normalised growth rate ($Im(\omega^*) \times 10^3$) as a function of the normalised wavenumber (k^*) in cold plasma regime ($c_{Se}^* = c_{Si}^* = 0$) for different propagation angles (θ). The key feature is a broad instability curve peaking at $k^* \approx 1.2$, with the growth rate being zero for all wavenumbers greater than a critical value of $k^* \approx 2.0$. The plot is largely insensitive to θ for larger k^* values, but for smaller k^* values ($k^* < 0.2$), significant deviations are evident from the plot's inset. As θ approaches $90°$, the onset of the instability is shifted and the growth rate is much weaker for longer wavelengths. This suggests that the magnetic field's influence is felt at fine scales for stabilisation of modes of lower frequency, but does not play a significant role for large scales in the overall streaming energy. At angles above $60°$, the inset reveals fine-scale structures where the growth rate is suppressed at low k^* before exhibiting a steeped, non-monotonic onset. This behaviour indicates that for near-perpendicular propagation, the magnetic restorative force effectively competes with the streaming drive to stabilise long-wavelength modes.

The polar plot in Fig. 3 displays the normalised growth rate as a function of both k^* and θ. A peak instability region (red) between $0.8 < k^* < 1.2$ is evident. The instability is widespread but slightly narrows and suppresses near $90°$, particularly at lower k^* values. This further confirms that while the streaming drive is largely isotropic, the magnetic field provides a subtle stabilising effect for perpendicular propagation. This isotropy is expected to break down in the presence of stronger magnetic fields.

Spectral characteristic profiles of the dispersion relation for the parallel streaming configuration ($\theta = 0°$) are shown in Fig. 4. It is to be noted that, for parallel streaming in the absence of thermal effects, Eq. 17 essentially reduces to a quartic polynomial as evident by the four modes shown in Fig. 4(a). The solid blue line (Mode 1) corresponds to high-frequency electrostatic branch, with Mode 4 corresponding to the weakly dispersive negative-frequency counterpart. The orange dashed (Mode 2) and yellow dotted (Mode 3) lines correspond to beam–plasma modes associated with the streaming-electron population. A reference line for the beam mode (solid black) is included to facilitate the identification of the beam-dominated branches in the dispersion plot. The nearly flat nature of the Mode 4, representing the backward-propagating mode, indicates minimal interaction with the forward-streaming beam.

However, Modes 2 and 3 show evidence of coupling (mode coalescence) in the wavenumber range $1.9 < k^* < 2.4$, which is the region of linear instability. This is evident from the growth rate region in Fig. 4(b), where the imaginary part of the frequency becomes non-zero. The peak normalised growth rate is found to be ~ 0.336 at $k^* = 1.1$.

The evolution of the characteristic plasma modes in variation with the ambient magnetic field is illustrated in Fig. 5. The invariance of the real frequency ($Re(\omega^*)$) modes with IMF is evident from the figure. For parallel streaming, IMF (B_0) is aligned with the streaming direction, hence field strength has no effect on the modes as well as the instability growth rate as shown in Figs. 5, 6. Mathematically, the term $\{\omega^{*2} - \Omega_i^{*2} \cos^2\theta\}$, for example, reduces to $\{\omega^{*2} - \Omega_i^{*2}\}$ in the Eq. 17. As a result, all terms containing Ω^* vanishes.

Profile in Fig. 7 illustrate the influence of the streaming-electron fraction (f_{eb}) on the instability growth rate. It is evident that the peak as well as the spread of the instability enhances with f_{eb}. The growth eventually vanishes for $f_{eb} = 0$. It establishes the stream-driven nature of the instability. Similar results have also been reported in the study on the streaming instability in Lorentzian dusty plasma (Paul et al. 2021).

Fig. 8 illustrates the spectral characteristic profiles of the dispersion relation for oblique streaming configuration ($\theta = 60°$). Eq. 17 reduces to a decic dispersion relation as evident from the presence of 10 modes in the Fig. 8(a). Compared to the $\theta = 0°$ case, six new modes (Modes 2,3,6-9) emerge in this case. Fig. 8(a) shows different branches representing different plasma wave modes. The highest frequency branch (Mode 1) is related to high-frequency electrostatic mode, where the frequency is finite at long wavelengths. It is shifted slightly upward due to the streaming effects. Low-frequency branches (Modes 4-9) near $\omega^* \approx 0$ correspond to acoustic modes, where the ion-acoustic mode is distinguished from the electron-acoustic mode based on the phase velocity (ω^*/k^*). Mode 5 represents a faster acoustic branch, consistent with electron-acoustic characteristics. Mode 4 shows clear deviation and bending near $k^* \sim 2$, indicating strong beam–plasma coupling and the formation of a beam-modified hybrid mode. Branches near $\omega^* \approx k^*$ are related to beam modes (Modes 2 & 3), while those near the beam modes but deviated are related to beam-modified modes resulting from beam-plasma interaction. These classifications are based on quantitative diagnostics of phase velocity (ω^*/k^*), closeness to the beam resonance condition $\omega^* \approx k^*$, and group velocity ($d\omega^*/dk^*$). A clear interaction can be seen between the modes 4 and 5 in the wavenumber region ~ 0.1 to ~ 2.0. These two modes (4 and 5) again exhibit coalescence in the subtle yet finite wavenumber range $k^* \sim 0 - 0.08$, which appears in the Fig. 8(b). These same wavenumber regions correspond to the onset of finite growth rates, as illustrated in the Fig. 8(c). The coincidence of mode merging, and the onset of growth indicates that the instability is triggered during the interaction of acoustic modes the beam mode. The instability attains its maximum around $k^* \approx 1.2$ with a peak growth rate of ~ 0.334.

The dependence of the real frequency ($Re(\omega^*)$) modes on the IMF (B_0) is illustrated in Fig. 9. In the absence of a magnetic field, the dispersion is dominated by linear beam-driven modes, but the introduction of even a weak field ($B_0 = 10\ nT$) triggers the emergence of new harmonic branches. As the field increases to $60\ nT$, these modes undergo significant splitting, where the degeneracy of the initial plasma oscillations is lifted. In the third panel, the horizontal lines at $Re(\omega^*) = 0$ are now very sharp and well separated. This suggests that for high B_0, a significant portion of the energy is localized in non-propagating or very slow modes.

Fig. 10 depicts the effects of the magnetic field (B_0) on the instability growth rate. The growth rate retains its characteristic bell-shaped dependence, with a maximum growth rate at $k^* \approx 1.25$. Although, it is found to remain relatively unaffected for lower magnetic fields ($B_0 = 10$ nT), increasing this value to 60 nT leads to a suppression in the maximum growth rate, as shown in the inset in Fig. 10. The suppression of this instability is small and can thus be interpreted that the magnetic field is damping this mode, possibly through confinement and limiting the energy transfer from the beam to the plasma. Furthermore, the small shift in k^* for 60 nT case indicates that stronger magnetic fields are more effective at damping long wavelength perturbations.

Fig. 11 reveals similar results with the Fig. 7. In this case ($\theta = 60°$) the secondary region of the instability along with the previous region also gets affected from the streaming-electron population.

Fig. 12(a) reveals the same modes as the Fig. 8(a). The transition from oblique propagation (Figs. 8(a), 8(b)) to perpendicular propagation (Fig. 12(a), 12(b)) is seen to display a change in the structure of the dispersion relation. For oblique propagation at 60°, the branches appear more spread-out with a smoother coupling over a large range of $k^*$and smoother interaction with the beam. Conversely, for perpendicular propagation the branches appear more compressed with sharper avoided crossing points and stronger clustering of low frequency branches at $Re(\omega^*) \approx 0$. The interaction with the beam is also seen to be more localized with respect to k^*, indicating stronger resonance effects. Thus, perpendicular propagation is seen to favour localized quasi-stationary structures, whereas oblique propagation favours broader spectral transport. Fig. 12(c) shows the growth rate associated with these modes. It is seen that while the secondary peak persists, it is reduced compared to the 60° case. It indicates a weaker secondary instability and a more localized energy distribution at 90°.

The Figs. 13-15 again verify the trends observed in Figs. (9-11) with a greater resolution of the angular dependence of the modes and a more detailed delineation of the instability region.

Figs. 17,18 are similar to Figs. 2, 3, but include the effects of finite thermal velocity of the species. In this case, Eq. 17 will be a 12-degree polynomial. In Fig. 18, the effect of thermal velocities is demonstrated by plotting both the cold case and the finite temperature case. In the finite temperature case, the instability is suppressed. This suggests that finite thermal velocity has a stabilizing effect on the streaming instability, consistent with the standard theory of streaming instabilities.

5 Observational validations

The numerical analysis reveals robust linear growth of electrostatic instabilities driven by a streaming-electron population over the LMAs. The dispersion relation analysis reveals a maximum growth rate (0.336) at $k^* \approx 1.1$, where the corresponding unnormalised real frequency ($Re(\omega^*)$) of the unstable mode is approximately 13 kHz. This frequency is close to the local electron plasma frequency (20 kHz) and lies within the 10-20 kHz Langmuir-wave band observed by *Kaguya* over the LMAs (Hashimoto et al. 2010). For a typical LMA region with a characteristic vertical extent of 50 km, the transit time for the streaming-electron population ($v_0 = 1.32 \times 10^7$ ms^{-1}) is approximately 3.79×10^{-3} s. The associated characteristic growth time (reciprocal of maximum growth rate) $\approx 2.27 \times 10^{-5}$ s is nearly two orders of magnitude shorter than the estimated electron transit time across the near-surface

region. This indicates that the unstable electrostatic modes can undergo significant amplification before the electrons traverse the interaction region (Chu et al. 2021), suggesting that the instability can efficiently develop within the spatial extent of the LMAs. Overall, these results provide theoretical support for the interpretation that the enhanced electrostatic activity observed over the LMAs is consistent with electron-streaming instabilities driven by mirror-reflected electron populations.

6 Conclusions

We have constructed a realistic model formalism to investigate the linear electron-streaming instability, excitable in magnetised three-component solar-wind plasmas, over the LMAs. By examining the generalised linear dispersion relation (Eq. 17) numerically, we reveal the sensitive dependence of the instability on the propagation angle relative to the IMF direction and the IMF strength. The instability is found to be largely isotropic across most wavenumbers, though near-perpendicular propagation ($\theta \geq 60°$, Fig. 2) introduces a non-monotonic onset, where the magnetic restorative force effectively stabilises the long-wavelength modes. It indicates the excitation of a preferred resonant mode scale, governed primarily by beam-plasma interaction rather than magnetic effects. The IMF plays a secondary, scale-dependent role, by subtly stabilising it. It primarily suppresses longer wavelength modes, especially for oblique and perpendicular propagations relative to the IMF (Fig. 2). Mode splitting and harmonic structures are evident in oblique cases (Figs. 8-9).

It is conjectured that the plasma system stabilises gradually with an increase in the IMF strength and vice-versa. The instability growth rate increases strongly with the streaming-electron fraction (f_{eb}) and then vanishes as this fraction approaches zero ($f_{eb} \to 0$, Fig. 7). It hereby confirms that this instability is sourced and powered by the streaming energy. In addition, thermal velocity act as a stabilising influence. Finite T_e and T_i reduce the instability growth rate and shrink the instability window (Fig. 18). Consequently, the cold plasma case represents an upper bound on the instability strength in terms of its growth features. Across all propagation angles, unstable regions coincide with the merging of dispersion branches, confirming a reactive streaming instability mechanism rather than a purely resonant one. Finally, the predicted excited wave frequency and the corresponding growth timescale are consistent with the *Kaguya* observations (Chu et al. 2021). It hereby reliably checks the physical viability of the proposed instability mechanism in the near-surface lunar plasma environment.

The presented analysis is restricted to a one-dimensional linear framework for mathematical tractability, assuming alignment between wave propagation and particle streaming. The adopted fluid model is appropriate for investigating the collective mode characteristics only. The validity of the fluid approximation is supported by the separation between the characteristic instability wavelength and the microscopic Debye scale. For the considered parameter regime, the long-wavelength approximation ($k\lambda_D \ll 1$) is satisfied. It indicates that the instability develops on scales larger than the Debye length, where charge separation effects remain small and the plasma response can be described through fluid moments. This analysis portrays the collective dispersion properties of the unstable electrostatic modes excited by electron-streaming instability. The kinetic effects associated with velocity-space resonances, particle trapping, and the nonlinear electron-hole formation

are beyond the scope of the present study. A more precise investigation incorporating all such effects and refinements certainly remains an important direction for future investigation.

Acknowledgements The authors sincerely acknowledge the members of the Astrophysical and Nonlinear Dynamics Research Laboratory (APNDRL), Department of Physics, Tezpur University, for insightful interactions. The institutional fellowship received by P.P.D. from Tezpur University is gratefully acknowledged. Lastly, IUCAA (Pune, India) associateship awarded to P.K.K. is duly acknowledged.

Author contributions P.P.D. wrote the manuscript, prepared the figures and performed the mathematical analysis, P.K.K. administered the project and contributed in critical analysis, revision and editing of the manuscript. P.K.K. handled the online submission of the manuscript.

Funding information No funds or grants were received for this work.

Data availability No new data has been generated in this study.

Declarations

Competing interests The authors declare that they do not have any conflict of interest regarding the preparation and publication of the presented study.

References

Aggarwal, S.: Two-stream instability in plasmas with arbitrary orientation of magnetic field. Astrophysics and Space Science. 66, 341–348 (1979)

Bamford, R.A., Kellett, B., Bradford, W.J., Norberg, C., Thornton, A., Gibson, K.J., Crawford, I.A., Silva, L., Gargaté, L., Bingham, R.: Minimagnetospheres above the Lunar Surface and the Formation of Lunar Swirls. Phys. Rev. Lett. 109, 081101 (2012). https://doi.org/10.1103/PhysRevLett.109.081101

Blewett, D.T., Coman, E.I., Hawke, B.R., Gillis-Davis, J.J., Purucker, M.E., Hughes, C.G.: Lunar swirls: Examining crustal magnetic anomalies and space weathering trends. Journal of Geophysical Research: Planets. 116, (2011)

Chen, F.: Introduction to plasma physics and controlled fusion. Springer (2015)

Chu, F., Halekas, J.S., Cao, X., McFadden, J.P., Bonnell, J.W., Glassmeier, K. -H.: Electrostatic Waves and Electron Heating Observed Over Lunar Crustal Magnetic Anomalies. JGR Space Physics. 126, e2020JA028880 (2021). https://doi.org/10.1029/2020JA028880

Cid, C., Saiz, E., Guerrero, A., Palacios, J., Cerrato, Y.: A Carrington-like geomagnetic storm observed in the 21st century. J. Space Weather Space Clim. 5, A16 (2015). https://doi.org/10.1051/swsc/2015017

Coleman Jr, P.: Subsatellite Magnetometer Experiment. Apollo 16: Preliminary Science Report. 315, (1972)

Dolginov, S.S., Eroshenko, E., Zhuzgov, L., Pushkov, N., Tyurmina, L.: Magnetic measurements on the second cosmic rocket. ARS Journal. 31, 1640–1644 (1961)

DOLGINOV, S.S., Yeroshenko, E., Zhuzgov, L., Pushkov, N.: Investigation of the magnetic field of the Moon. AIAA Journal. 1, 514–516 (1963)

Garrick-Bethell, I., Weiss, B.P., Shuster, D.L., Buz, J.: Early lunar magnetism. Science. 323, 356–359 (2009)

Halekas, J., Brain, D., Lin, R., Mitchell, D.: Solar wind interaction with lunar crustal magnetic anomalies. Advances in Space Research. 41, 1319–1324 (2008)

Halekas, J., Mitchell, D., Lin, R., Frey, S., Hood, L., Acuña, M., Binder, A.: Mapping of crustal magnetic anomalies on the lunar near side by the Lunar Prospector electron reflectometer. Journal of Geophysical Research: Planets. 106, 27841–27852 (2001)
Halekas, J., Saito, Y., Delory, G., Farrell, W.: New views of the lunar plasma environment. Planetary and Space Science. 59, 1681–1694 (2011)
Hapgood, M., Lockwood, M., Bowe, G., Willis, D., Tulunay, Y.: Variability of the interplanetary medium at 1 AU over 24 years: 1963–1986. Planetary and Space Science. 39, 411–423 (1991)
Hartmann, W.K., Davis, D.R.: Satellite-sized planetesimals and lunar origin. Icarus. 24, 504–515 (1975)
Hashimoto, K., Hashitani, M., Kasahara, Y., Omura, Y., Nishino, M.N., Saito, Y., Yokota, S., Ono, T., Tsunakawa, H., Shibuya, H., Matsushima, M., Shimizu, H., Takahashi, F.: Electrostatic solitary waves associated with magnetic anomalies and wake boundary of the Moon observed by KAGUYA. Geophysical Research Letters. 37, 2010GL044529 (2010). https://doi.org/10.1029/2010GL044529
Heiken, G., Vaniman, D., French, B.M.: Lunar sourcebook: A user's guide to the Moon. Cup Archive (1991)
Hood, L., Coleman Jr, P., Russell, C., Wilhelms, D.: Lunar magnetic anomalies detected by the Apollo substatellite magnetometers. Physics of the Earth and Planetary Interiors. 20, 291–311 (1979)
Hood, L., Schubert, G.: Lunar magnetic anomalies and surface optical properties. Science. 208, 49–51 (1980)
Hood, L., Vickery, A.: Magnetic field amplification and generation in hypervelocity meteoroid impacts with application to lunar paleomagnetism. Journal of Geophysical Research: Solid Earth. 89, C211–C223 (1984)
Hood, L.L., Artemieva, N.A.: Antipodal effects of lunar basin-forming impacts: Initial 3D simulations and comparisons with observations. Icarus. 193, 485–502 (2008)
Kasper, J., Lazarus, A., Gary, S., Szabo, A.: Solar wind temperature anisotropies. Presented at the AIP Conference Proceedings (2003)
Kivelson, M.G., Russell, C.T., Brown, M.E.: Introduction to space physics. (1996)
Kruparova, O., Krupar, V., Szabo, A., Lario, D., Nieves-Chinchilla, T., Martinez Oliveros, J.C.: Unveiling the interplanetary solar radio bursts of the 2024 Mother's Day solar storm. The Astrophysical Journal Letters. 970, L13 (2024)
Kurata, M., Tsunakawa, H., Saito, Y., Shibuya, H., Matsushima, M., Shimizu, H.: Mini-magnetosphere over the Reiner Gamma magnetic anomaly region on the Moon. Geophysical research letters. 32, (2005)
Labro, Q., Davoine, X., Gremillet, L., Bergé, L.: Simulating ultrarelativistic beam-plasma instabilities with a quasistatic particle-in-cell code. Computer Physics Communications. 324, 110140 (2026). https://doi.org/10.1016/j.cpc.2026.110140
Li, X., Temerin, M., Tsurutani, B., Alex, S.: Modeling of 1–2 September 1859 super magnetic storm. Advances in Space Research. 38, 273–279 (2006)
Lim 임, J.정훈, Simon, J.B., Li 李, R.日新, Brouillette, O., Rea, D.G., Lyra, W.: The Streaming Instability in 3D: Conditions for Strong Clumping. ApJ. 1000, 156 (2026). https://doi.org/10.3847/1538-4357/ae47e9
Lin, R., Anderson, K., Hood, L.: Lunar surface magnetic field concentrations antipodal to young large impact basins. Icarus. 74, 529–541 (1988)
Lin, R., Mitchell, D., Curtis, D., Anderson, K., Carlson, C., McFadden, J., Acuna, M., Hood, L., Binder, A.: Lunar surface magnetic fields and their interaction with the solar wind: Results from Lunar Prospector. Science. 281, 1480–1484 (1998)
Lue, C., Futaana, Y., Barabash, S., Wieser, M., Holmström, M., Bhardwaj, A., Dhanya, M., Wurz, P.: Strong influence of lunar crustal fields on the solar wind flow. Geophysical Research Letters. 38, (2011)
Mack, K.: Magnetic Fields Explain Lunar Surface Features. Physics. 5, 92 (2012)
Maksimovic, M., Zouganelis, I., Chaufray, J., Issautier, K., Scime, E.E., Littleton, J., Marsch, E., McComas, D., Salem, C., Lin, R.: Radial evolution of the electron distribution functions in the fast solar wind between 0.3 and 1.5 AU. Journal of Geophysical Research: Space Physics. 110, (2005)
Parker, E.N.: Dynamics of the interplanetary gas and magnetic fields. Astrophysical Journal, vol. 128, p. 664. 128, 664 (1958)

Paul, S., Denra, R., Sarkar, S.: Study of two stream instabilities in Lorentzian dusty plasma. Physics of Plasmas. 28, (2021)
Richardson, I.G., Cane, H.V.: Near-Earth interplanetary coronal mass ejections during solar cycle 23 (1996–2009): Catalog and summary of properties. Solar Physics. 264, 189–237 (2010)
Richmond, N., Hood, L.: A preliminary global map of the vector lunar crustal magnetic field based on Lunar Prospector magnetometer data. Journal of Geophysical Research: Planets. 113, (2008)
Runcorn, S.K.: The early magnetic field and primeval satellite system of the Moon: clues to planetary formation. Philosophical Transactions of the Royal Society of London. Series A: Physical and Engineering Sciences. 349, 181–196 (1994)
Saito, Y., Yokota, S., Tanaka, T., Asamura, K., Nishino, M., Fujimoto, M., Tsunakawa, H., Shibuya, H., Matsushima, M., Shimizu, H.: Solar wind proton reflection at the lunar surface: Low energy ion measurement by MAP-PACE onboard SELENE (KAGUYA). Geophysical Research Letters. 35, (2008)(a)
Saito, Y., Yokota, S., Tanaka, T., Asamura, K., Nishino, M., Fujimoto, M., Tsunakawa, H., Shibuya, H., Matsushima, M., Shimizu, H.: Solar wind proton reflection at the lunar surface: Low energy ion measurement by MAP-PACE onboard SELENE (KAGUYA). Geophysical Research Letters. 35, (2008)(b)
Su, W.-S., Smallwood, J.L., Lin, M.-K., Yang, C.-C., Cuello, N.: Evolution of dust in a protoplanetary disc driven by stellar flybys: implications for the streaming instability. Monthly Notices of the Royal Astronomical Society. 547, stag173 (2026). https://doi.org/10.1093/mnras/stag173
Takahashi, F., Tsunakawa, H.: Thermal core-mantle coupling in an early lunar dynamo: Implications for a global magnetic field and magnetosphere of the early Moon. Geophysical Research Letters. 36, (2009)
Thomas, B.T., Smith, E.J.: The Parker spiral configuration of the interplanetary magnetic field between 1 and 8.5 AU. Journal of Geophysical Research: Space Physics. 85, 6861–6867 (1980)
Tsunakawa, H., Shibuya, H., Takahashi, F., Shimizu, H., Matsushima, M., Matsuoka, A., Nakazawa, S., Otake, H., Iijima, Y.: Lunar magnetic field observation and initial global mapping of lunar magnetic anomalies by MAP-LMAG onboard SELENE (Kaguya). Space Science Reviews. 154, 219–251 (2010)
Wurz, P.: Solarwind composition. Presented at the The Dynamic Sun: Challenges for Theory and Observations (2005)

Figures:

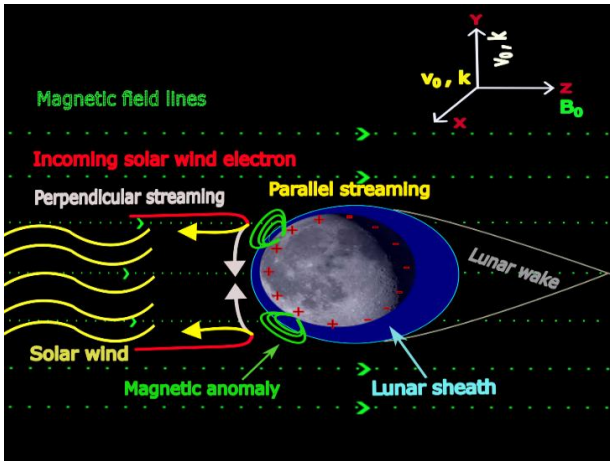


Fig. 1 A schematic cartoon depicting the solar wind plasma interaction with the LMAs. Yellow and grey lines respectively show parallelly and perpendicularly reflected streaming-electron beams. The green dotted lines in the background depict the IMF lines.

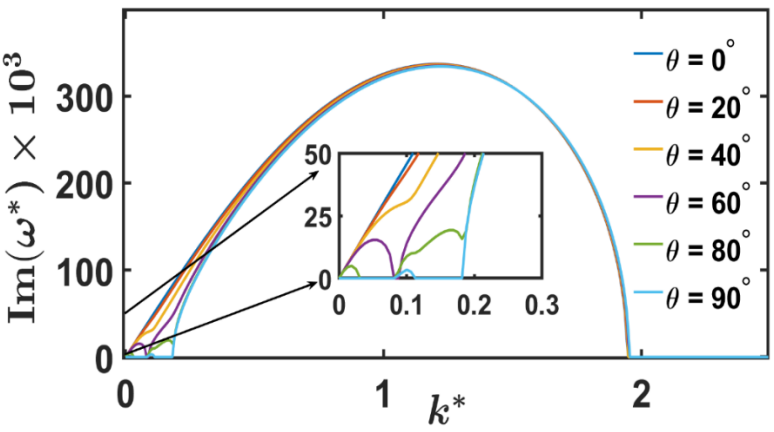


Fig. 2 Profile of the normalised growth rate ($\mathrm{Im}(\omega^*) \times 10^3$) associated with various indicated streaming angles (θ) plotted against the normalised wavenumber (k^*) in the absence of thermal effects ($c_{Se}^* = c_{Si}^* = 0$).

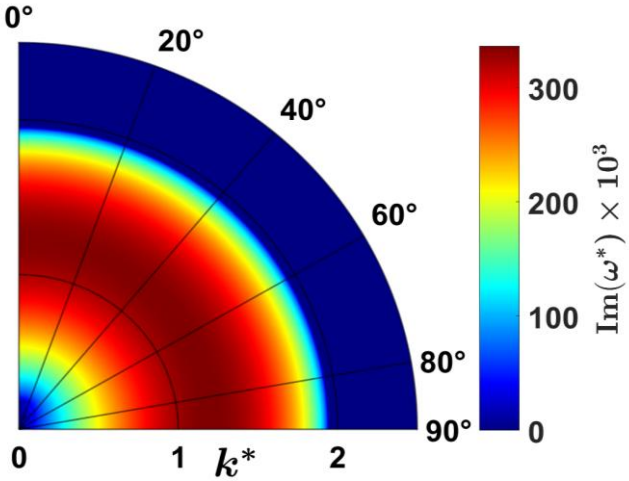


Fig. 3 Polar colour map illustrating the normalised growth rate ($\mathrm{Im}(\omega^*) \times 10^3$) as a function of the normalised wavenumber (k^*) and the streaming angle (θ). The radial lines indicate the k^*–magnitude and θ is measured clockwise from the vertical axis. The colour intensity scale depicts the spectral distribution of the instability across the (k^*, θ) plane.

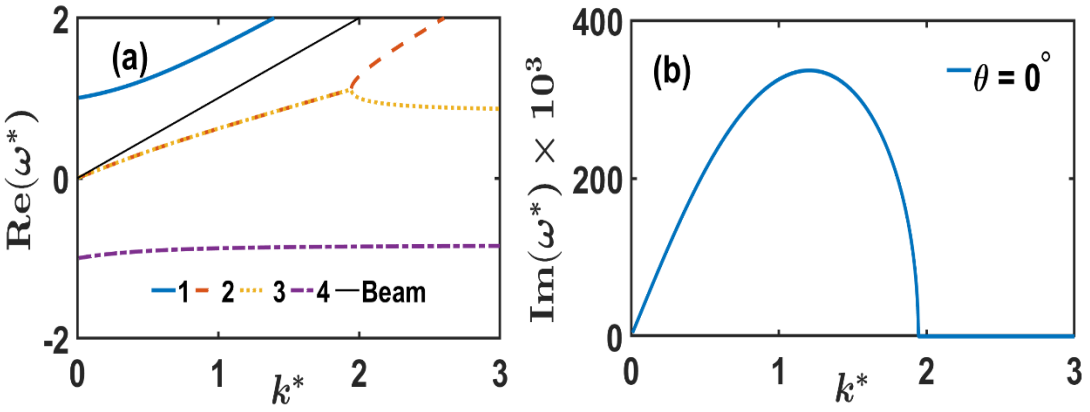


Fig. 4 Spectral characteristic profiles of the dispersion relation for the parallel streaming configuration ($\theta = 0°$), showing **(a)** Various real frequency ($\mathrm{Re}(\omega^*)$) modes in variation with wavenumber (k^*), and **(b)** The corresponding growth rate ($\mathrm{Im}(\omega^*) \times 10^3$), illustrating the unstable bandwidth and the dominant mode of the system.

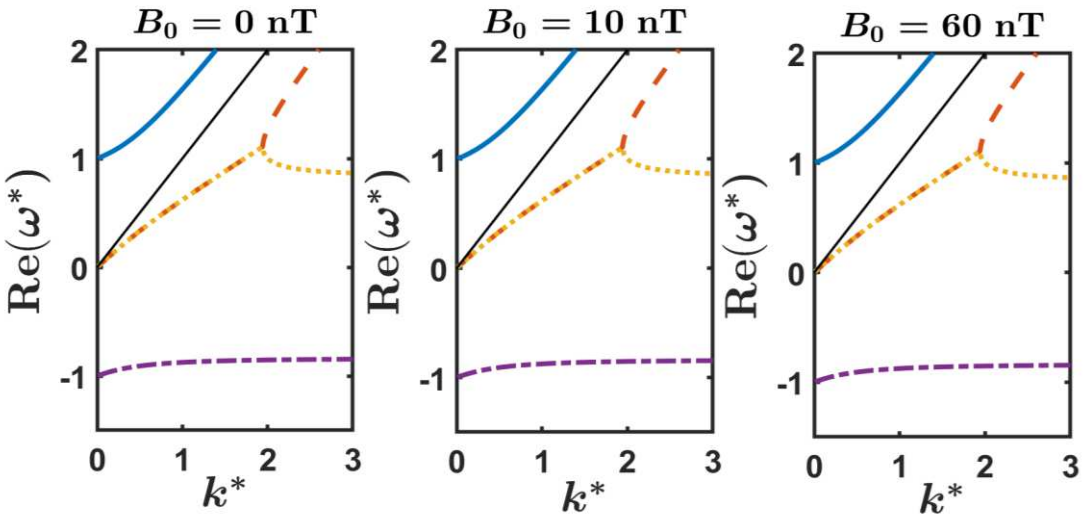


Fig. 5 Profile showing the evolution of the characteristic plasma modes as the ambient magnetic field (gyrofrequency) is varied. It illustrates invariance of the real frequency ($\mathrm{Re}(\omega^*)$) modes with respect to the IMF (B_0).

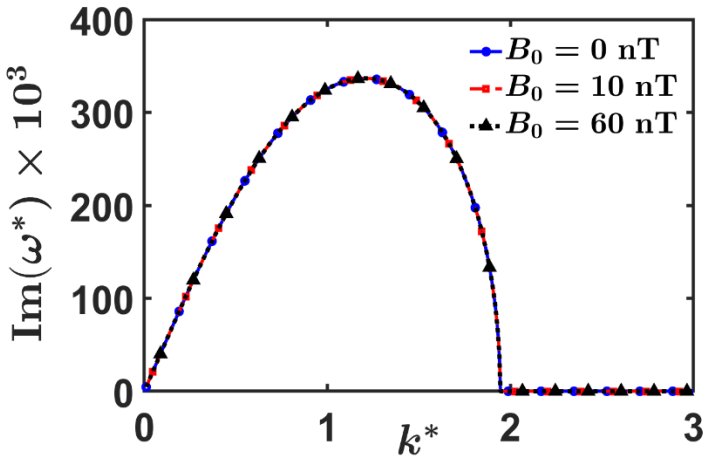


Fig. 6 Profile illustrating invariance of the growth rate ($\mathrm{Im}(\omega^*) \times 10^3$) with respect to the magnetic field strength (B_0) in parallel streaming ($\theta = 0°$) configuration.

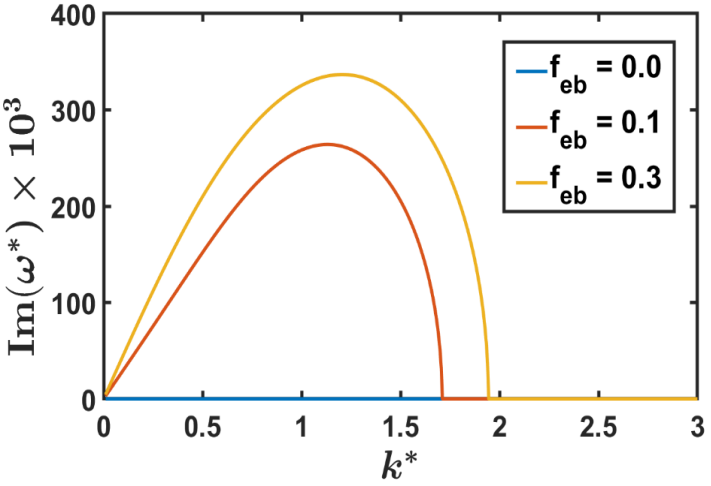


Fig. 7 Profile illustrating the influence of the streaming-electron fraction (f_{eb}) on the instability growth rate ($\mathrm{Im}(\omega^*) \times 10^3$).

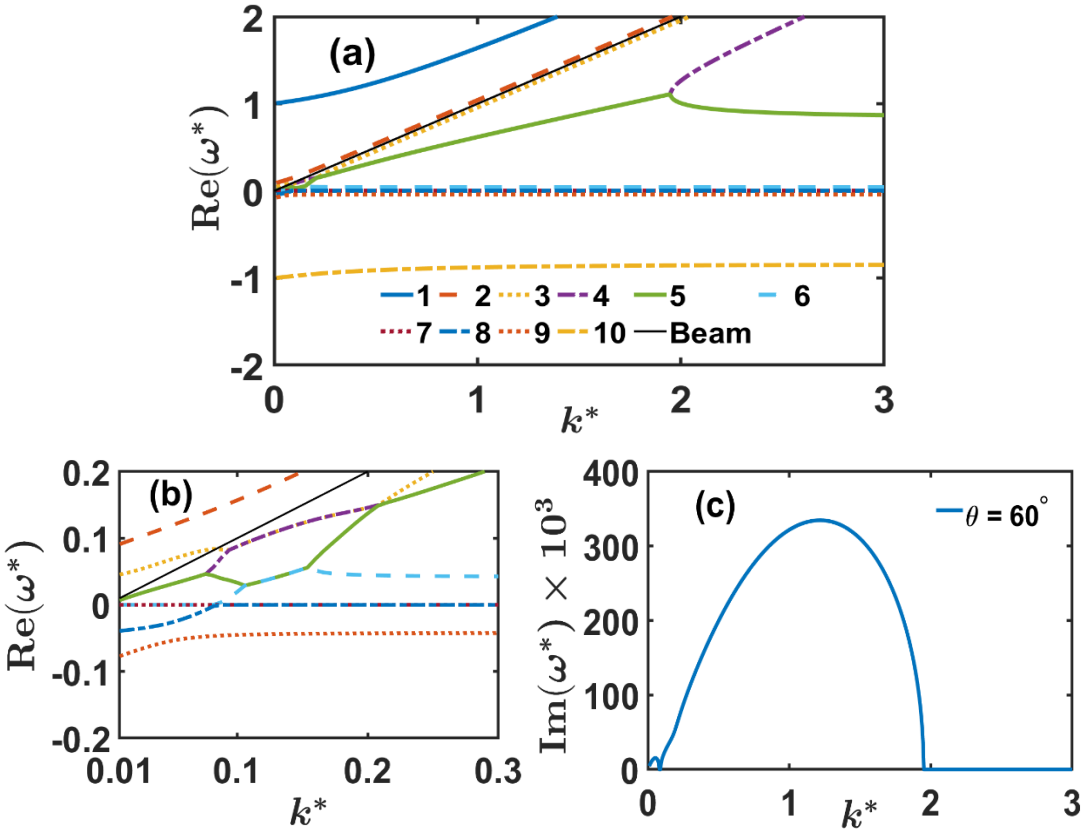


Fig. 8 Spectral characteristic profiles of the dispersion relation for oblique streaming configuration ($\theta = 60°$) showing **(a)** Various real frequency ($\mathrm{Re}(\omega^*)$) modes in variation with the wavenumber (k^*), **(b)** Magnified detail of the curves presented in (a), and **(c)** The corresponding instability growth rate ($\mathrm{Im}(\omega^*) \times 10^3$).

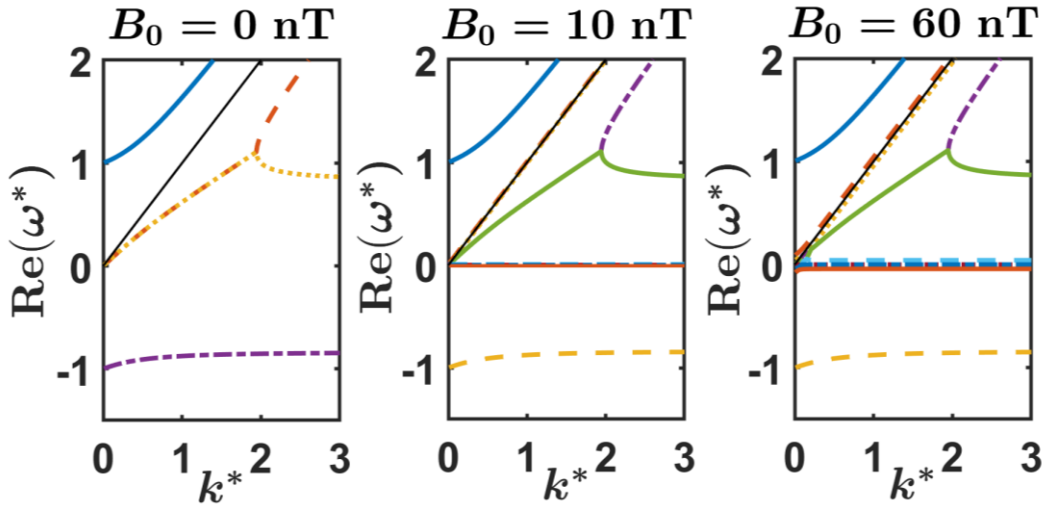


Fig. 9 Same as Fig. 5 but for oblique propagation ($\theta = 60^{\circ}$). It illustrates the dependence of the real frequency ($\mathrm{Re}(\omega^*)$) modes on the IMF (B_0).

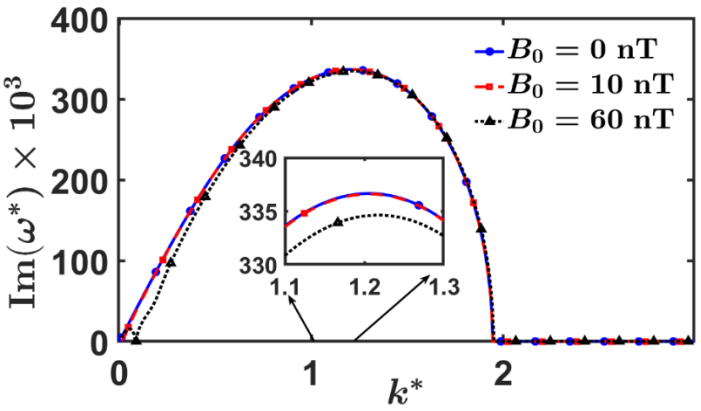


Fig. 10 Same as Fig. 6, but for oblique propagation ($\theta = 60^{\circ}$). Finite variation of the instability growth rate ($\mathrm{Im}(\omega^*) \times 10^3$) with field strength ($B_0$) is illustrated.

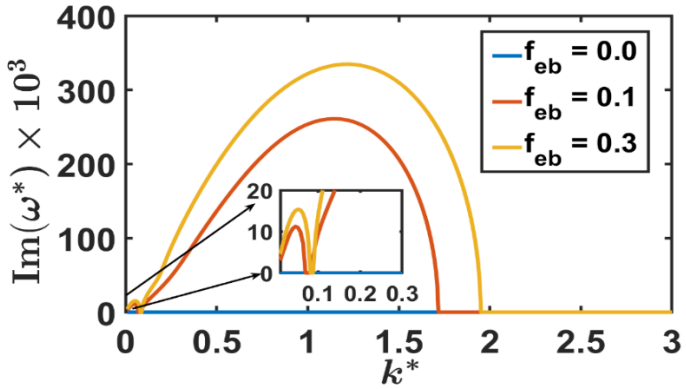
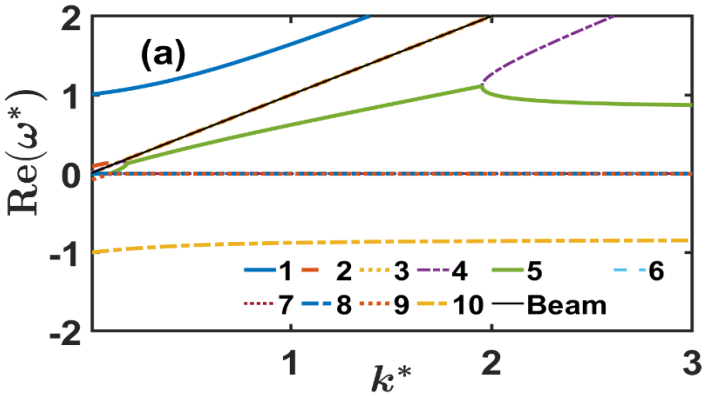


Fig. 11 Same as Fig. 7, but for oblique propagation ($\theta = 60^{\circ}$).



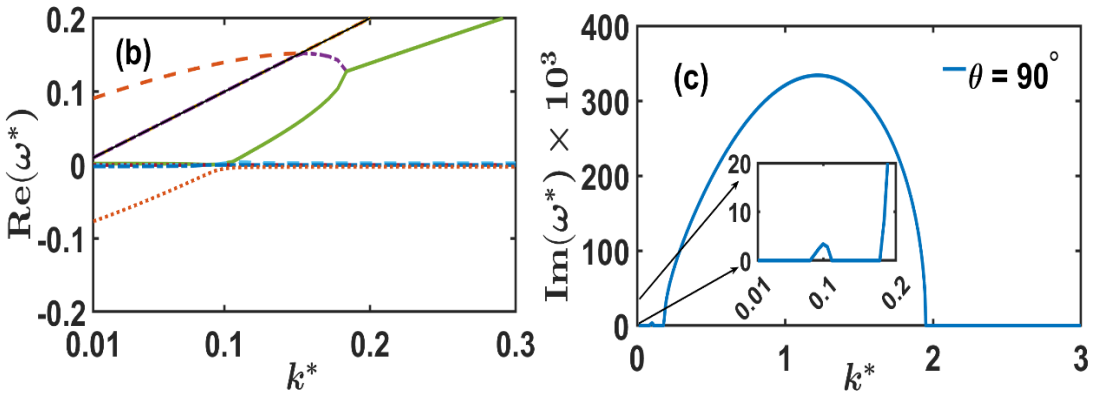


Fig. 12 Same as Fig. 8, but for perpendicular streaming ($\theta = 90^{\circ}$). It illustrates the emergence of new modes along with a new unstable bandwidth compared to the parallel case ($\theta = 0^{\circ}$).

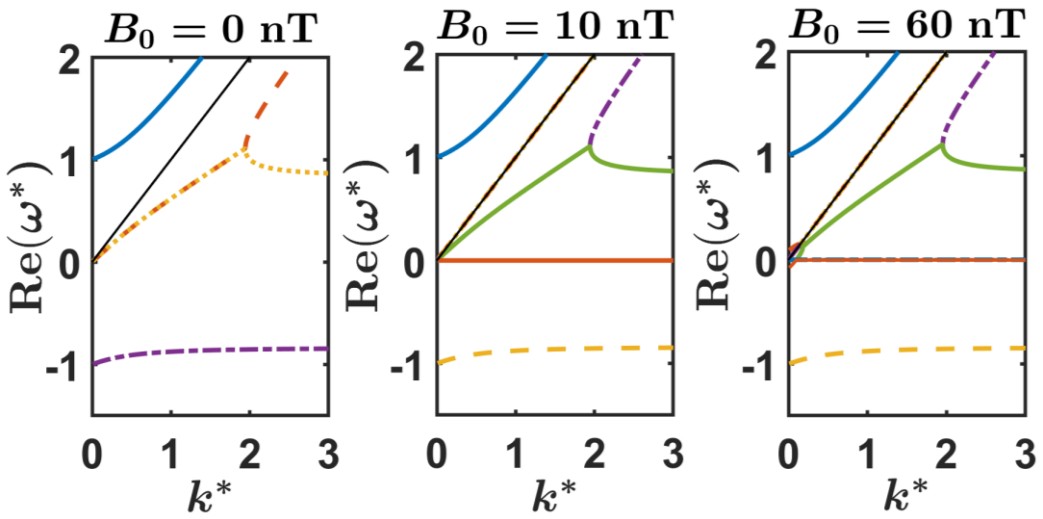


Fig. 13 Same as Fig. 5, but for perpendicular propagation ($\theta = 90^{\circ}$). It illustrates dependence of the real frequency ($\mathrm{Re}(\omega^*)$) modes on the IMF (B_0).

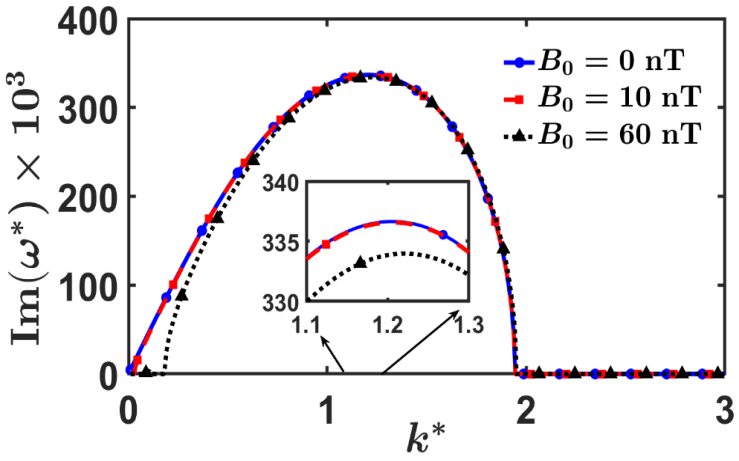


Fig. 14 Same as Fig. 6, but for perpendicular propagation ($\theta = 90^{\circ}$). Finite variation of the instability growth rate ($\mathrm{Im}(\omega^*) \times 10^3$) with field strength ($B_0$) is illustrated.

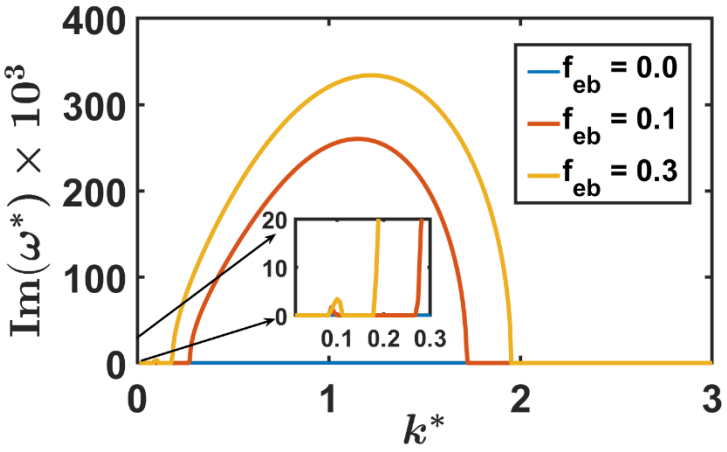


Fig. 15 Same as Fig. 7, but for perpendicular propagation ($\theta = 90^{\circ}$).

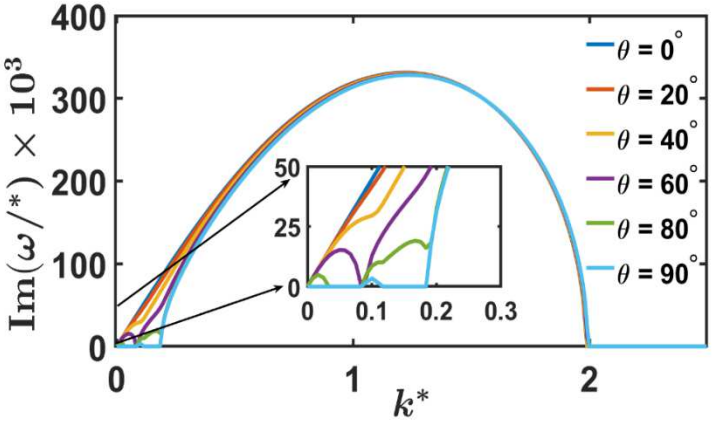


Fig. 16 Same as Fig. 2, but for finite thermal velocities ($c_{Se}^* = 0.10, c_{Si}^* = 0.00074$).

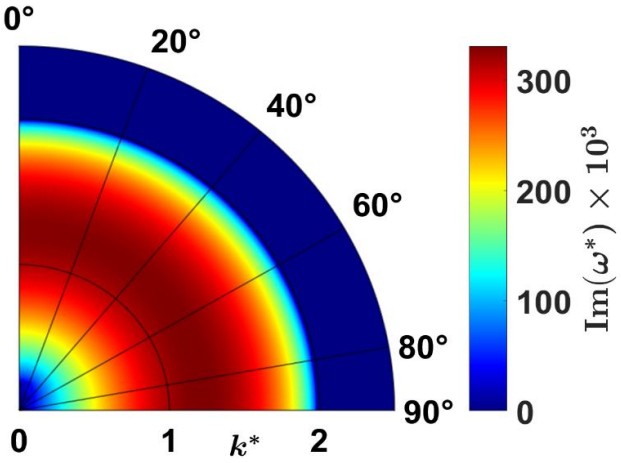


Fig. 17 Same as Fig. 3, but for finite thermal velocities ($c_{Se}^{*} = 0.10, c_{Si}^{*} = 0.00074$).

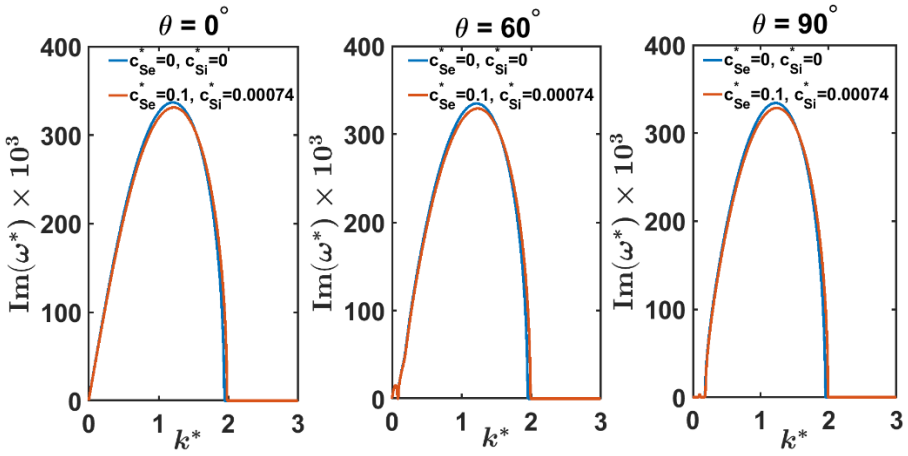


Fig. 18 Profile of the instability growth rate ($\mathrm{Im}(\omega^{*}) \times 10^{3}$) associated with cold electron-proton and hot electron-proton population for **(a)** $\theta = 0^{\circ}$, **(b)** $\theta = 60^{\circ}$, and **(c)** $\theta = 90^{\circ}$.